

Compressed Sensing (CS) Imaging with Wide FOV and Dynamic Magnification

Final Report

Award no: N00014-07-1-0393
Award period: 12/10/06-6/15/10
Sponsor: Office of Naval Research
March 14, 2011

ONR Program manager:

Dr. Michael Duncan, Program Officer
Electro-Optics/Infrared Sensor Processing
Office of Naval Research
ONR Department Code: 312
875 North Randolph Street
Arlington, VA 22203-1995

Tel: (703) 696-5787
Fax: 703-696-1331
michael.d.duncan2@navy.mil

**Principal Investigator and
Technical Point of Contact:**

Gonzalo R. Arce, Charles Black Evans Professor
Department of Electrical and Computer Engineering
University of Delaware
Newark, DE 19716

Tel: (302) 831-1493
Fax: (302) 831-4316
arce@ece.udel.edu
www.ee.udel.edu/~arce

Co-Principal Investigators:

Dennis W. Prather, College of Engineering Alumni Professor
Department of Electrical and Computer Engineering
University of Delaware
Newark, DE 19716

Tel: (302) 831-8170
Fax: (302) 831-4316
dprather@ee.udel.edu
www.ee.udel.edu/~dprather

20110321633

In the Compressed Sensing (CS) Imaging with Wide FOV and Dynamic Magnification Project Report we present the development of diverse imaging systems based on Compressive Sensing or Compressive Sampling (CS) method. In particular, we demonstrate three different implementations of the CS-based imaging systems, including: (a) a single pixel camera, (b) a CS-based multispectral imaging system, and (c) a CS-based optical sectioning microscope (CSM).

1 Single Pixel Camera

Most optical images are sparse in some transformed domains, such in the Fourier or Wavelet domain. To exploit the sparse information in the transformed domain, we used CS measurement patterns to modulate the intensity of optical images. Based on the CS measurement results, the original optical image can be reconstructed by solving a minimization problem. To experimentally realize the CS measurement process, we utilized a Digital Micromirror Device (DMD) to implement the CS measurement patterns. The core component of the DMD is a 768(V) \times 1024(H) aluminum micromirror array. Each mirror can be electrically driven to be turned on or off. The DMD is installed in the image plane of an objective lens. When CS measurement patterns are being displayed by the DMD, in its reflection direction, we can see the intensity of optical images modulated by the active DMD pattern. The CS measurements are collected into a single pixel detector by a focusing lens. Since only a single pixel detector is used to acquire the complete information of the optical image, this CS-based imaging system design can also be considered as a single pixel camera. Figure 1 shows the schematic drawing of the single pixel camera.

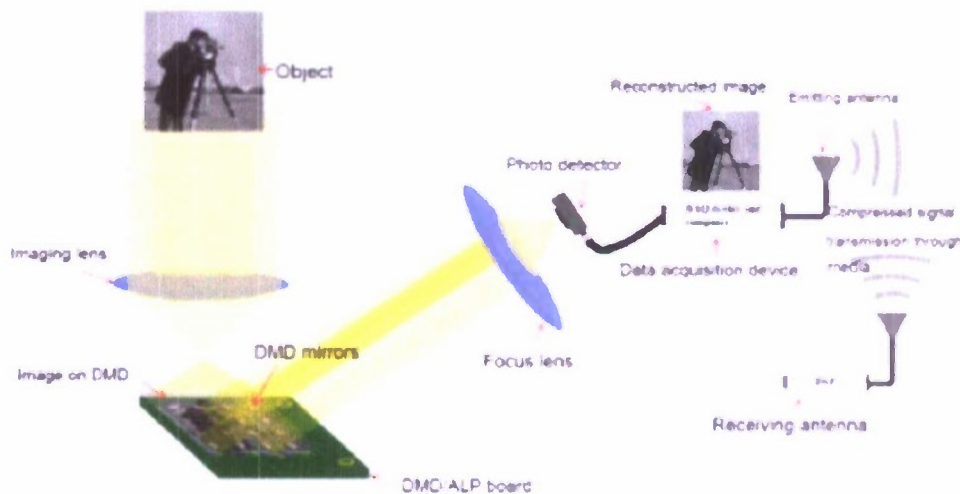


Figure 1: Schematic drawing of the DMD-based single pixel camera.

Figure 2(a) shows the experimental setup of the single pixel camera. Figure 2(b), (c), and (d) show one of the CS measurement patterns used in our experimental setup, its DMD implementation, and an image-modulation result by the DMD pattern, respectively.

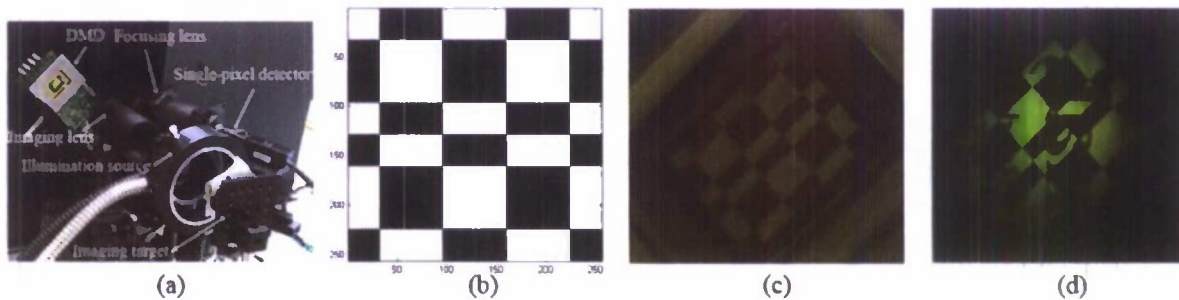


Figure 2: (a) The experimental realization of a single pixel camera. (b) A CS measurement pattern. (c) The DMD implementation of the CS measurement pattern. (d) An image-modulation result using the DMD implemented CS measurement pattern.

Figure 3 shows an image reconstruction result obtained from our experimental setup. Fig 3(a) shows a CCD image of the imaging target, which is a piece of paper printed with two characters. Figures 3(b) shows the reconstructed image of the imaging target. In this experiment, we used a variable density sampling method in the Hadamard domain to realize the CS measurement process. The reconstructed image has a pixel size of 256×256 , and it was reconstructed using 6554 CS measurement results. In this result, we can see that the important information of the imaging target was successfully reconstructed.

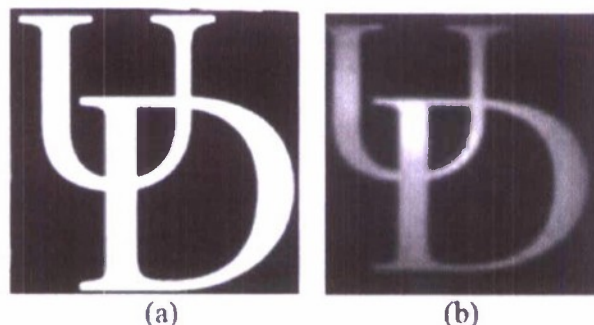


Figure 3: (a) A CCD image of the imaging target. (b) An image reconstruction result generated using our experimental setup.

The single pixel camera can also be used to realize passive CS imaging in the near infrared (NIR) spectrum. Figure 4 shows the reconstructed optical images in the wavelengths of 1200 nm (Fig. 4(b)) and 1450 nm (Fig. 4(c)). Figure 4(a) shows the imaging target, which is a USAF-1951 resolution target. In this experiment, NIR Light Emitting Diodes (LEDs) of emission wavelengths of 1200 nm and 1450 nm were used for illumination and a single pixel Germanium (Ge) detector was used to collect the CS measurements.

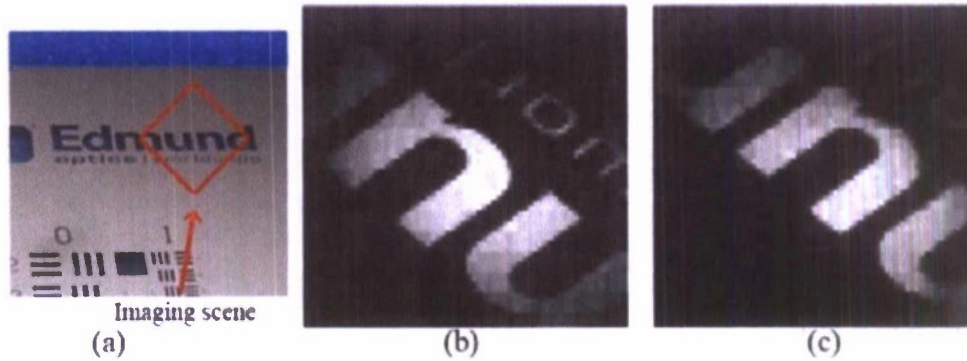


Figure 4: (a) Imaging target. (b) Optical image reconstructed in the wavelength of 1200 nm. (c) Optical image reconstructed in the wavelength of 1450 nm.

2 Compressive Sampling Multispectral Imaging System

The hardware architecture of the single pixel camera can be conveniently extended to build a CS-based Multi-Spectral Imaging (CS-MSI) system. Conventional MSI systems usually use sensor-arrays or single pixel detectors plus mechanical scanning instruments to acquire optical images at multiple spectral channels. In a CS-MSI system, expensive sensor-arrays or complicated mechanical scanning instruments can be avoided and only single pixel detectors are needed to acquire images at multiple spectral channels. This means the economic/technical investments on MSI systems can be significantly reduced.

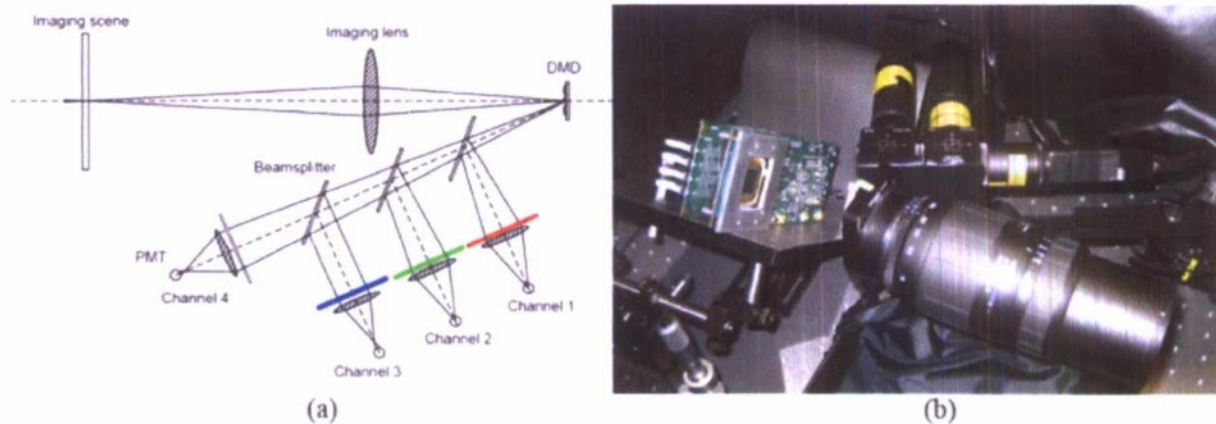


Figure 5: Schematic drawing of a 4-channel CS-MSI system.

Figure 5 shows the schematic drawing of the CS-based MSI (CS-MSI) system. In this design, the DMD-reflected image irradiance was split into four spectral channels by beamsplitters. Different spectral filters were installed at the end of the spectral channels. Three visible wavelength bandpass filters, centered at 650 nm, 550 nm and 450 nm were used at channels-1, 2, and 3, respectively. At channel-4, a 1200-nm long-pass filter was used to isolate the NIR spectral information. The transmission bandwidth of the 450-nm filter is 40

nm whereas the 550-nm and 650-nm spectral filters had a transmission bandwidth of 10 nm. In the NIR spectral channel (Channel-4), a single pixel detector based on Ge material was used. In the visible spectral channels, photomultiplier tubes (PMT) were used. The imaging target was a color checker card (X-Rite Mini ColorChecker). A 150-W quartz halogen lamp (Dolan-Jenner DC-950H DC-Regulated Fiber Optic Illuminator) was used to illuminate the imaging target, along with a 150-W Xenon lamp (Newport Research Arc Lamp Source) to enhance the illumination in the UV and NIR spectrums when needed. Figure 6 shows an image reconstruction results obtained using our setup (the top row images), which are compared with CCD images captured using the same spectral filters as the ones installed in the CS-MSI system (the bottom row images). CCD images are scaled and resized to match the reconstructed images. No brightness/contrast adjustment was applied to the displayed images.

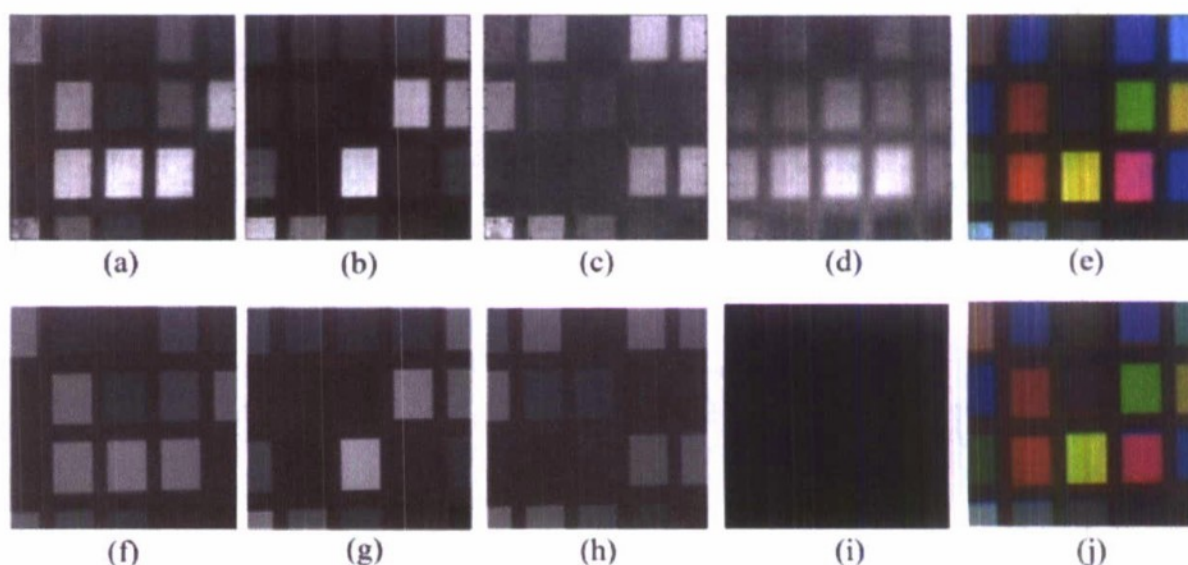


Figure 6: Comparison between the spectral images reconstructed from the CS-MSI testbed (top row) and CCD spectral images captured with the same filters (bottom row). (a) (b), (c) and (d) are spectral images reconstructed from the 650-nm, 550-nm, 450-nm and NIR spectral channels respectively. (f), (g), (h) and (i) are CCD images captured with the 650-nm, 550-nm, 450-nm and the NIR spectral filters respectively. (e) Color image reconstruction result, which is generated by filling the visible spectral images into an RGB data format. (j) RGB synthesis of the CCD visible spectral images.

Figures 6 (a), (b), (c) and (d) are spectral images reconstructed in the 650-nm, 550-nm, 450-nm and NIR spectral channels. Figures 6 (f), (g), (h) and (i) are CCD images captured with the 650-nm, 550-nm, 450-nm and the 1200-nm long-pass filters. In Fig. 6 (i), we do not see any useful information because the CCD camera used in this experiment was not sensitive to wavelengths in the NIR spectrum. To capture these CCD spectral images, the DMD in the CS-MSI system was replaced with an exposed CCD sensor array (AVT PIKE F-100C). Spectral filters were placed directly in front of the exposed CCD. Figure 6 (e)

is generated by filling the images reconstructed from the visible spectral channels into an RGB data format. Figure 6 (j) is the corresponding RGB synthesis of CCD spectral images. The reconstructed images shown in Fig. 6 have a pixel size of 256×256 (65536 pixels). The Hadamard-space variable-density sampling method was used and the down-sampling ratio was 10% (6534 CS measurements).

3 Compressive Sampling Optical Sectioning Microscope

In this effort, we also implemented the CS method in building optical sectioning for confocal microscopy imaging systems. In conventional optical sectioning microscopes, optical sections are captured using a single pixel detector, such as a Photo Multiplier Tube (PMT), in a point-by-point fashion. To acquire the complete information from the imaging scene, usually a 2-axis scanning process is needed. This scanning process can be time consuming. To reduce the image acquisition time, a novel design called Programmable Array Microscope (PAM) was proposed. PAM systems use a DMD to implement multi-pinhole masks in conjugate image planes of a confocal microscope. Compared to conventional optical sectioning microscopes, the image acquisition speed of PAM systems is much faster, because in this case, the information from multiple points in the imaging scene is acquired at the same time. In PAM systems, CCD cameras are used to acquire the confocal information from the imaging target. In low light or high speed imaging settings, CCD cameras pose high economic and technical challenges to the PAM system. If CS measurement patterns are implemented with the PAM system, confocal images can be captured by single pixel detectors and thus the technical/economic investments on CCD cameras in PAM systems can be reduced. PAM systems implemented with CS measurement patterns can be considered as Compressive Sensing Microscopes or CSMs. Figure 7 shows the schematic drawing of the CSM system.

Figure 8 shows our experimental realization of the CSM system and one of the image reconstruction results obtained using this experimental setup. The imaging target used in this experiment is a slide of skin section. The objective lens used in this setup is a 60x Olympus lens, with a Numeric Aperture (NA) of 0.85. A 532 nm solid state laser (30 mW) was used for illumination. We implemented the Hadamard space variable density sampling method in order to realize the CS measurement process and we also used 6534 measurement patterns in this experiment. The reconstructed image had a pixel size of 128×128 . The excitation filter used in this experiment had a center wavelength of 543 nm. Its transmission bandwidth was 30 nm. The emission filter had a center wavelength of 610 nm and a transmission bandwidth of 75 nm. In the experiment, we used Modified Scrambled-Block Hadamard Ensembles (MSBHEs) as measurement patterns. The measurement patterns had a pixel size of 128×128 . The block size (BS) of the MSBHE patterns was 16.

Figure 9 shows a wide field multispectral microscopic image reconstruction result (2 spectral channels) obtained using the experimental setup. Figure 9 (a) is the imaging target captured by a CCD camera. The imaging target was a 15- μ m fluorescent beads slide. Figure 9 (b) shows the multispectral image reconstruction result captured by our experimental setup. Figure 9 (c) shows the green spectral image of the imaging target, which was captured under the illumination of a 532 nm solid state laser. The fluorescent filter set used to capture this

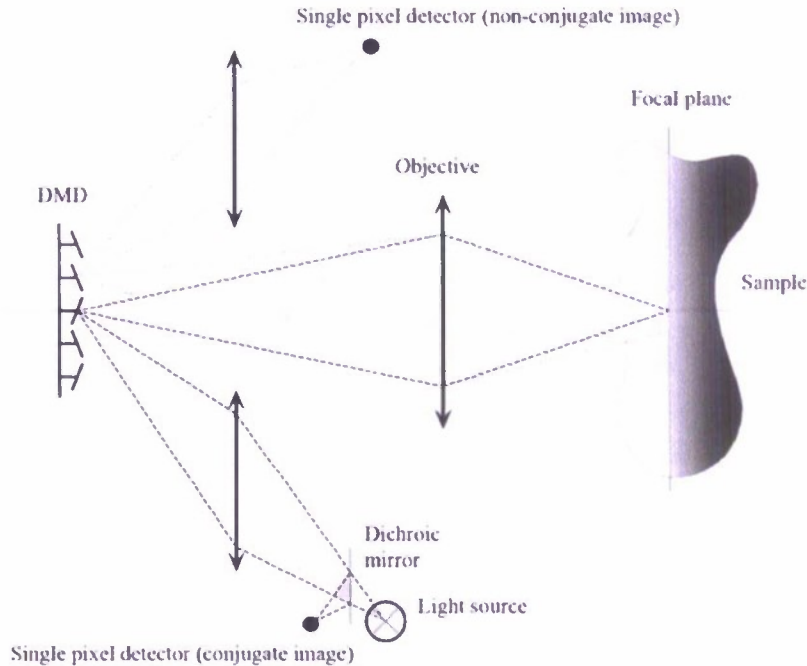


Figure 7: Schematic drawing of the CSM system.

spectral image was: excitation filter (center wavelength (nm)/bandwidth (nm)): 543/30, emission filter: 610/75. Figure 9 (d) shows the red spectral image, which was captured with a 632 nm when a He-Ne laser was used. The fluorescent filter set used to capture this spectral image was: excitation filter (center wavelength (nm)/bandwidth (nm)): 620/60, emission filter: 700/75. The filter sets are purchased from Chroma.

We also studied the optical sectioning imaging performance of the CSM system. Figure 10 shows 6 optical sections of a reflective imaging target (a microcircuit chip) reconstructed using our experimental setup. In this experiment, we used a white light source (Dolan-Jenner DC-950H DC-Regulated Fiber Optic Illuminator) for illumination.

Figure 10(a) shows the imaging target. Figures 10(b) – (g) show the reconstructed optical sections. The adjacent optical sections are $1\mu\text{m}$ away from each other. We can see the reconstructed information of the imaging target changes as the optical section moves in the depth direction. Figure 11 shows another set of optical sectioning imaging results captured using the experimental setup. In this case, a biological specimen (pollen grain) was used as the imaging target. A 532 nm solid state laser was used for illumination. The excitation filter used in this experiment had a center wavelength of 543 nm, and a bandwidth 30nm. The emission filter had a center wavelength of 610nm, and a bandwidth of 75nm. The image in the top-left corner is the imaging target, which is a wide-field image captured using a CCD camera and white light illumination. The right side images are the reconstructed optical sections of the imaging target. The adjacent optical sections are $1\mu\text{m}$ away from each other in the depth direction. From this result, we can see that as the optical section moves in the depth direction, different information of the pollen grain specimen in the depth direction was reconstructed.

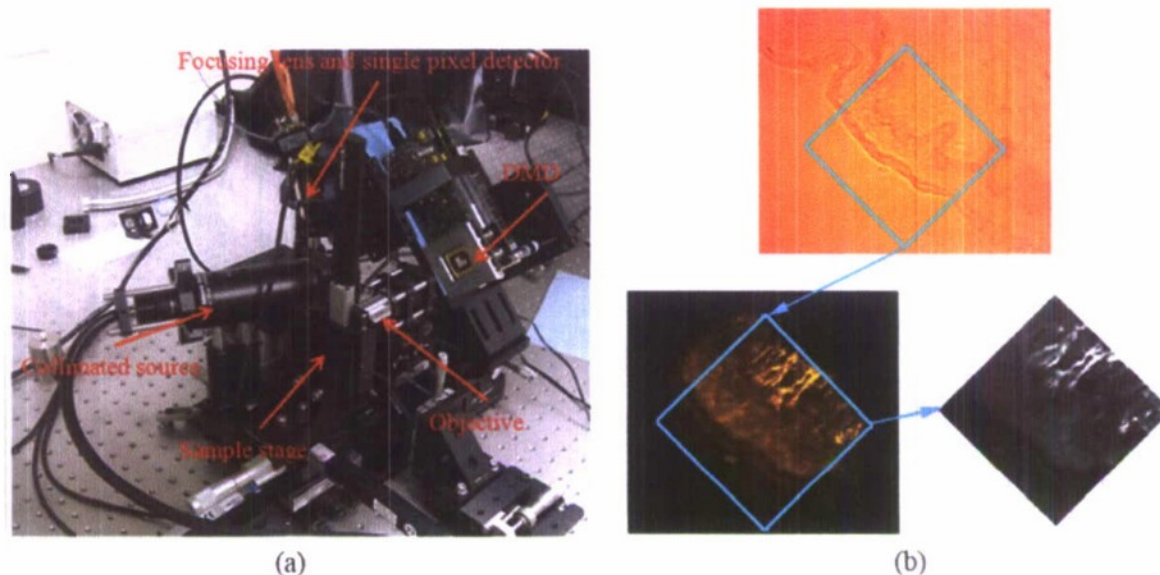


Figure 8: (a) Experimental setup of the CSM system. (b) Biological sample (skin section) reconstruction result from a compressive sampling PAM setup.

4 Reconstruction Algorithm

By exploiting the sparsity of natural images, compressed sensing has shown that it is feasible to acquire and reconstruct natural images from a limited number of linear projection measurements at sub-Nyquist sampling rates [1, 2]. A key to the success of CS is the design of the measurement ensemble, which is based on the evaluation of the incoherence between the measurement ensemble and the sparsity basis. The incoherence property requires that the components of the measurement ensemble should have dense representations in the sparsity basis. Due to the large scale nature of images, the generation of the measurement ensemble should be both computationally efficient and memory efficient. Furthermore, the sampling scheme should enable fast algorithms to perform image reconstruction.

Measurement matrices where each entry is an independent and identically distributed (i. i. d.) random variable obeying Gaussian or Bernoulli distribution have been proposed for compressed image sampling [1, 2]. Recently, it has been shown that the performance of CS sampling can be improved if the random measurement matrices are suitably optimized [3]. These methods lead to optimized but unstructured measurement matrices and thus large memory space and computation demanding resources are needed, making them prohibitively expensive for implementation. A more desirable way to obtain linear measurements is by incoherent sampling in a transform domain that is equipped with fast transform algorithms [4]. Measurement ensembles in the transform domain that enable fast computations include partial Fourier ensemble, scrambled Fourier ensemble (SFE), scrambled block Hadamard ensemble (SBHE) and Noiselets. These have been shown to obtain good performance in CS applications [2, 4, 5]. With the exception of signal sparsity on a given basis, however, the formulation of these sampling approaches does not exploit any *a priori* information of natural images that could lead to improved CS performance [6, 7].

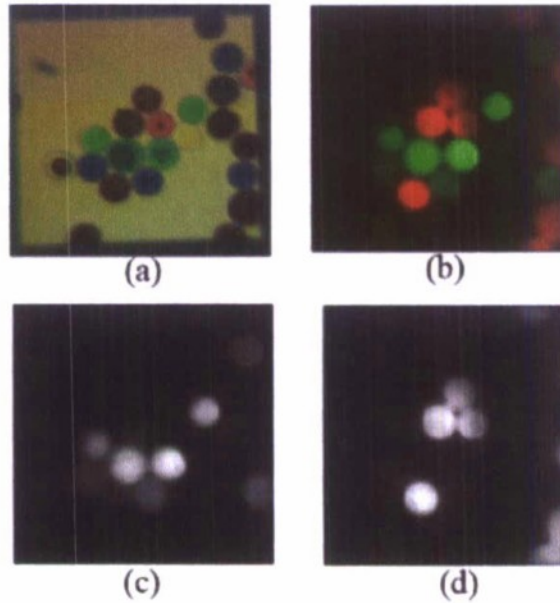


Figure 9: (a) Imaging target used in this experiment, which is a fluorescent bead specimen. The diameter of the beads is 15- μ m. (b) Multispectral image-reconstruction result obtained from the experimental setup (2 spectral channels). (c) Spectral image reconstructed when a 532 nm solid state laser was used to offer illumination. The fluorescent filter set used to capture this spectral image is: excitation filter (center wavelength (nm)/bandwidth (nm)): 543/30, emission filter: 610/75. (d) Spectral image reconstructed when a 632 nm He-Ne laser was used for illumination. The fluorescent filter set used to capture this spectral image is (excitation filter: 620/60, emission filter: 700/75).

We developed a method to effectively exploit such *a priori* information in the design of efficient CS measurement ensemble by using the inherent statistical distributions that natural images exhibit in the sparse wavelet domain. A novel family of variable density sampling patterns are designed in the frequency transform domain, which is applicable to the Discrete Fourier Transform (DFT), Discrete Cosine Transform (DCT) and ordered discrete Hadamard transform (DHT) [8]. To design the proposed measurement matrices, the widely used generalized Gaussian distribution (GGD) model is adopted to statistically describe the distribution of image wavelet coefficients. The method of incoherent Fourier sampling of subband wavelets proposed in [4] provides an efficient way to acquire sparse subband wavelets in the DFT domain. The Fourier coefficients in the band where significant energy of the wavelet exists are sampled randomly to minimize the coherence between the sparse wavelets and the measurement Fourier atoms. Based on such incoherent Fourier subband sampling strategy, we derive a variable density sampling function $p(m, n)$ in the frequency transform domain according to the adopted statistical wavelet model. Here $p(m, n)$ indicates the probability that the (m, n) th coefficient is sampled. The design of the variable density sampling function is then further improved so that not only the distribution of significant wavelet coefficients are considered, but also their rapid magnitude decay from coarse scales to fine scales. The sampling patterns in the frequency transform domain are generated

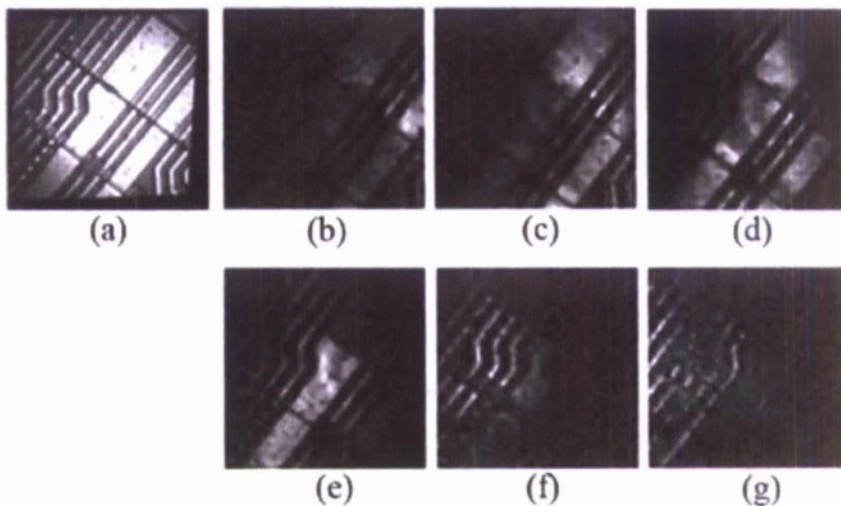


Figure 10: Optical sectioning imaging result. (a) Imaging target captured by a CCD camera, which is a microcircuit chip. (b)-(g) Optical sections reconstructed from our experiment testbed. The distance between two adjacent optical sections in the depth direction is $1\mu\text{m}$.

randomly according to the underlying probability function.

Equipped with fast transform algorithms, the proposed sampling processes are simple, fast and can be easily implemented. By exploiting the *a priori* information of natural images, the CS performance obtained with the proposed sampling method is significantly improved. Compared with other sampling patterns, such as radial sampling pattern and variable density spiral that also exploit some *a priori* information of the images [2, 7], the proposed sampling patterns are not heuristically constructed, but are based on reliable statistical models of wavelet coefficients and thus the proposed sampling patterns are analytically justified.

4.1 Background Reconstruction Algorithm

4.1.1 Compressed Sensing in a Transform Domain

A signal $\mathbf{x} \in \mathcal{R}^N$ is S sparse on some basis $\Psi = [\underline{\psi}_1, \underline{\psi}_2, \dots, \underline{\psi}_N]$ if \mathbf{x} can be represented by a linear combination of S vectors of Ψ with $S \ll N$. The signal can be expressed as: $\mathbf{x} = \Psi \underline{\theta}$, where $\underline{\theta}$ is an $N \times 1$ vector with only S non-zero entries. Compressible signals, such as natural images, can also be well described by such sparse signal model [9]. Here we consider compressed image sampling in the transform domain Φ . To obtain the sparse signal information, we acquire a small set of transform coefficients of \mathbf{x} in Φ . The measurements are given by: $\mathbf{y} = \Phi_\Omega \mathbf{x}$, where Φ_Ω is a $M \times N$ matrix with $M \ll N$ and $\mathbf{y} = [y_1, y_2, \dots, y_M]^T$ represents the M measurements. Each row of Φ_Ω , $\underline{\phi}_i$, is taken from a subset $\Omega \subset \{1, \dots, N\}$ of the atoms of Φ . If Ψ and Φ are incoherent with each other and $\underline{\phi}_i$ is randomly chosen, then \mathbf{x} can be recovered from \mathbf{y} with high probability when M satisfies: $M = CS \log N \ll N$, where $C \geq 1$ is the oversampling factor [1, 2]. The incoherence between two bases (Ψ, Φ) is characterized by the mutual coherence defined as: $\nu(\Psi, \Phi) = \sup\{|\langle \psi, \phi \rangle| : \psi \in \Psi, \phi \in \Phi\}$ [10]. It is found that the low coherence property holds for many pairs of bases (Ψ, Φ).

In practical applications where noise is present, the measurements are modeled as: $\mathbf{y}_n =$

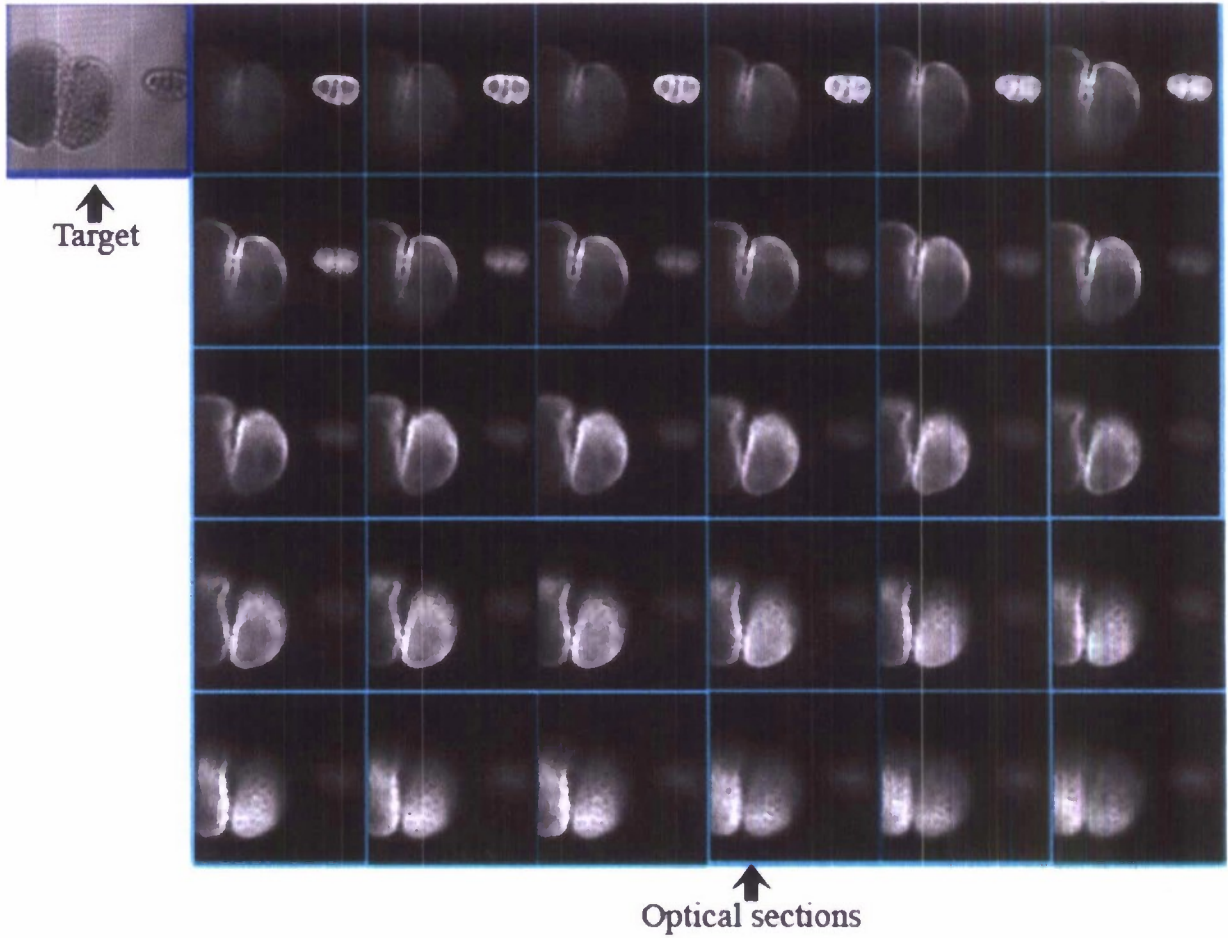


Figure 11: Optical sectioning imaging result of a pollen grain specimen. The distance between adjacent optical sections in the depth direction is $1\mu m$.

$\Phi_{\Omega}\Psi\theta + \mathbf{n}$, where \mathbf{n} is zero-mean additive white Gaussian noise. The reconstructed signal can be obtained by using the Basis Pursuit Denoising (BPDN) algorithm which solves the following problem [11]:

$$\hat{\theta} = \arg \min_{\theta} \|\Phi_{\Omega}\Psi\theta - \mathbf{y}_n\|_2^2 + \lambda\|\theta\|_1, \quad (1)$$

where $\|\theta\|_1 = \sum_i |\theta_i|$ and $\lambda > 0$ depends on the noise level. Note that BPDN works equally well for the approximate reconstruction of compressible signals [11]. If there exist fast algorithms associated with both Φ and Ψ , then a fast reconstruction algorithm can be implemented for signal reconstruction [4].

4.1.2 Incoherent Fourier Sampling of Sparse Wavelet Subbands

Wavelets have well defined spectral characteristics in the Fourier domain [12]. A coarse scale wavelet has its spectrum localized in the low frequency band whereas a fine scale wavelet has its spectrum widely spread out in the high frequency band. In [4], it is observed that if the signal to be acquired is restricted to a certain wavelet subband, a set of incoherent

measurements can be obtained by selecting the Fourier coefficients from the corresponding frequency band where significant energy of the wavelet exists.

Let $k = 1, 2, \dots, K$ denote the scale of the 1D wavelets where $k = 1$ is the finest scale and $k = K$ is the coarsest scale. Without loss of generality, it is assumed that the wavelet has length $N = 2^K$. Let $\varphi_{k,l}$ denote the 1D wavelet at a scale k with a shift $l \in [0, N2^{-k} - 1]$, then the DFT spectrum of $\varphi_{k,l}$ is over the band $\mathcal{B}_k = [-N2^{-k}, -N2^{-k-1}] \cup [N2^{-k-1}, N2^{-k}]$. To reconstruct $\varphi_{k,l}$ from its DFT samples, the DFT atoms are randomly selected within the band \mathcal{B}_k [4]. Assume the number of significant wavelets over \mathcal{B}_k is S_k , then approximately $2S_k$ to $3S_k$ Fourier measurements are needed. The probability that a DFT atom is sampled depends on the size of \mathcal{B}_k and on the sparsity S_k . Since smooth signals have most of their significant wavelet components clustered in the coarse scales, incoherent Fourier subband sampling implies that the low frequency Fourier coefficients, which contain much of the signal's energy, should be sampled with higher probability ¹.

The principle of Fourier sampling of wavelet subbands can be readily applied to 2D images. Assume the underlying image is of size $N \times N$. Let $\varphi_{k,i,j}^B$ denote the (i, j) th 2D wavelet at the k th scale of subband B where $B \in LH, HL, HH$, $i, j = 0, \dots, N_k - 1$ and $N_k = N/2^k$. The DFT spectrum of all the wavelets at the k th scale can be characterized by $\bar{\mathcal{B}}_k = ([-N2^{-k}, -N2^{-k-1}] \cup [N2^{-k-1}, N2^{-k}]) \times ([-N2^{-k}, -N2^{-k-1}] \cup [N2^{-k-1}, N2^{-k}])$. Again, the probability that a 2D DFT atom within $\bar{\mathcal{B}}_k$ is sampled depends on the size and on the number of significant wavelets of $\bar{\mathcal{B}}_k$.

4.2 Variable Density Sampling in the Fourier Domain

4.2.1 Variable Density Sampling Functions

For 2D natural images, the significant wavelet components tend to cluster around coarse scales. Thus, according to the principle of Fourier sampling of wavelet subbands, the Fourier coefficients to be measured should also cluster over low frequency bands. Obviously, by placing the samples selectively but still in a random manner, we can achieve better quality of image reconstruction than if those measurements are chosen uniformly random. In the following, we discuss how the sampling probability of the Fourier samples should change over different frequency bands.

For natural images, it is well-known that the distribution of wavelet subband coefficients can be adequately described by GGD models [13]. Let $w_{i,j,k}^B$ denote the (i, j) th wavelet coefficient in the k th scale. For ease of analysis, we assume that $w_{i,j,k}^B$, for $B \in LH, HL, HH$, belongs to the same GGD with the probability density function given by:

$$f(x; \sigma_k, \beta_k) = \eta(\sigma_k, \beta) \exp\{-[|x|/d(\sigma_k, \beta_k)]^{\beta_k}\}, \quad (2)$$

where $d(\sigma_k, \beta_k) = \sigma_k \sqrt{\frac{\Gamma(1/\beta_k)}{\Gamma(3/\beta_k)}}$, $\eta(\sigma_k, \beta_k) = \frac{\beta_k}{2\Gamma(\frac{1}{\beta_k})d(\sigma_k, \beta_k)}$ and $\Gamma(z) = \int_0^\infty t^{-1+z} e^{-t} dt$ is the Gamma function. The parameters σ_k and β_k are the standard deviation and the shape parameter of the k th scale, respectively. Typical values of β_k for natural images falls in the

¹Results in [4] do not directly imply that if multiple subbands contain nonzero elements and the corresponding frequency intervals are sampled proportionally to their occupancy, the signal can still be recovered with high probability. Thus, splitting the signal into various wavelet subbands and then performing incoherent sampling is suggested.

range [0.5, 1] [13]. The variance of the k th scale wavelet coefficients is given by σ_k^2 which is assumed to decrease exponentially from coarse scales to fine scales [14]:

$$\sigma_k^2 = 2^{-a(K-k)}, \quad (3)$$

where $a > 0$. It was shown in [14] that a can range from 2.25 to 3.1 based on the inference from empirical studies. Equation (3) also reveals the fact that the magnitude of wavelet coefficient decays rapidly from coarse scales to fine scales. Here the coarsest scaling coefficient of the image is assumed to belong to a uniform distribution $U(0, 1)$.

We first discuss how the sampling probability of DFT atoms should change according to the incoherent sampling of wavelet subbands. Here we define the significant wavelet coefficients as the wavelet coefficients whose magnitudes are larger than a threshold $\mu > 0$. Since the number of wavelet coefficients at scale k is $3(4^{K-k})$, the mean of the number of significant wavelet coefficients at scale k is:

$$\lambda_k = 6(4^{K-k}) \int_{\mu}^{\infty} f(x; \sigma_k, \beta_k) dx. \quad (4)$$

Consider the (m, n) th DFT atom within the band $\bar{\mathcal{B}}_k$ corresponding to the wavelet scale $k = K - \lfloor \log_2(2s) \rfloor$ where $s = \max\{|m|, |n|\}$ and $-N/2 \leq m, n < N/2$. It is clear that the number of DFT atoms within $\bar{\mathcal{B}}_k$ satisfies: $\varsigma_k \propto 4^{K-k}$. Thus, based on the incoherent Fourier subband sampling method, the probability that the (m, n) th DFT atom is selected also satisfies:

$$\tilde{p}(m, n) \propto \frac{\lambda_k}{\varsigma_k} \propto \int_{\mu}^{\infty} f(x; \sigma_k, \beta_k) dx. \quad (5)$$

Before examining $\tilde{p}(m, n)$ in the general case it is insightful to consider a special case of the GGD: the Laplacian ($\beta_k = 1$). The Laplacian distribution is of particular importance for the following two reasons: 1) it is analytically more tractable; 2) the empirical distribution of subband wavelets for many natural images are close to Laplacian [13]. With $\beta_k = 1$ and $d(\alpha_k, \beta_k) = \sigma_k/\sqrt{2}$, it can be shown that:

$$\int_{\mu}^{\infty} f(x; \sigma_k, \beta_k) dx = \frac{1}{2} \exp\left(-\frac{\sqrt{2}\mu}{\sigma_k}\right). \quad (6)$$

Thus, $\tilde{p}(m, n)$ can be approximated as:

$$\tilde{p}(m, n) \propto \exp\left[-\left(2^{\frac{a+1}{2}} \mu s^{\frac{a}{2}}\right)\right]. \quad (7)$$

It is clear that $\tilde{p}(m, n)$ decays exponentially along with the atom coordinates s and the decay rate depends on the image characteristic parameter a . Analysis based on the Laplacian distribution indicates that in the general case, $\tilde{p}(m, n)$ should also decay exponentially with its atom coordinates. For the random selection of DFT atoms, it is convenient to construct a sampling density function in the DFT domain and generate a sampling pattern according to the sampling density function. Designing a sampling density function following (7) would require image dependent parameter a , β_k and μ . However, in reality, only the number of measurements J is known. A method which does not require image dependent information to design an effective sampling density function is more desirable.

To conform to the decaying behavior of the sampling probability with increasing coordinates while keeping a simple form, we propose a new family of sampling density functions containing only exponential terms. Assuming the size of the underlying image is $M \times N$, the probability that the (m, n) th coefficient is sampled is given by:

$$p_F(m, n) = \exp \left[-\frac{(\sqrt{(\frac{m}{N})^2 + (\frac{n}{N})^2})^{a_F}}{\sigma_F^2} \right], \quad (8)$$

where $-M/2 \leq m < M/2$ and $-N/2 \leq n < N/2$. $a_F > 0$ is a parameter characterizing the decay of the sampling probability. $\sigma_F > 0$ is a parameter tuned to obtain the desired number of samples. Since $0 < p_F(m, n) < 1$, $p_F(m, n)$ is suitable as a probability function. Furthermore, the proposed sampling density function is flexible to accommodate various decaying rates and different number of measurements by tuning the parameters a_F and σ_F . Given a_F , the sampling ratio defined as J/MN is a monotonically increasing function of σ_F . Thus, the search of σ_F for a desired number of measurements is straightforward. Furthermore, σ_F can also be found by numerically solving the following problem:

$$\int_{-\frac{1}{2}}^{\frac{1}{2}} \int_{-\frac{1}{2}}^{\frac{1}{2}} \exp \left[-\frac{(\sqrt{x^2 + y^2})^{a_F}}{\sigma_F^2} \right] dx dy = \frac{J}{M \times N}. \quad (9)$$

The sampling patterns generated from the sampling density function are binary where 1 at (m, n) indicates a sampling point and 0 means no measurement on that point is made. With a probability given by $p_F(m, n)$, 1 will be generated at (m, n) ; otherwise, 0 will be generated.

Based on the observation from the case of the Laplacian distribution, it is reasonable to set $a_F = \frac{1}{2}a\bar{\beta}$, where $\bar{\beta}$ is defined as the averaged value of several coarsest scale shape parameters. However, it should be noted that the above analysis based on the incoherent Fourier subband sampling principle only provides approximately equal probability of reconstruction for significant wavelet components both at coarse scales and at fine scales. For image reconstruction, the contribution of an individual significant wavelet component to the image quality should be considered. Equation (3), along with empirical data analysis, reveals that a significant wavelet coefficient at a coarse scale usually has much larger magnitude than that of a significant wavelet coefficient at a fine scale. Thus, probabilistically, a coarse scale wavelet has much more contribution to the reconstructed image quality than that of a fine scale wavelet. Consequently, to achieve good reconstructed image quality, it is desirable to give more preference to the reconstruction of coarse scale wavelet components. Such intuitive analysis shows that an effective sampling density function should decay faster than predicted by $a_F = \frac{1}{2}a\bar{\beta}$ and it is desirable to increase the decaying parameter a_F away from $\frac{1}{2}a\bar{\beta}$. Simulation results show that $a_F \approx 1.3 a$ leads to good image reconstruction, as will be illustrated in Sec. 4.4. It is also observed that the quality of the reconstructed image is robust to variations of a_F if a_F is sufficiently large. If an estimation of a is not available, then setting $a_F = 3.5$ is recommended since this value leads to robust and satisfactory CS performance.

4.2.2 Variable Density Sampling Spiral for MRI

The variable density sampling pattern proposed in Sec. 4.2.1 can be applied to MRI in k -space, leading to a reduced set of measurements. However, this method does not necessarily reduce the total scan time. For MRI applications that have limited scan time, like functional MRI, a single-shot spiral pattern can effectively cover the k -space within one repetition time (T_R) period [15].

Based on the proposed variable density sampling function $p_F(m, n)$, a single-shot spiral sampling pattern is designed which involves two steps. In the first step, starting from the

origin of the k -space, the proposed spiral samples all the points within radius γ on the sampling grid. For a given threshold $0 < t_h < 1$, γ is set such that $p_F(m, n) > t_h$ for $\sqrt{m^2 + n^2} < \gamma$. In the second step, where $\sqrt{m^2 + n^2} \geq \gamma$, the trajectory of the spiral is described by the polar equation:

$$r(t) = \exp(bt^{a_F}), \quad \left(\frac{\ln \gamma}{b}\right)^{\frac{1}{a_F}} \leq t \leq \left(\frac{\ln \frac{N}{2}}{b}\right)^{\frac{1}{a_F}}, \quad (10)$$

where $b > 0$ and N is the size of the sampling grid in the k -space. The parameter t is sampled sufficiently so that the sampling points are continuously located along the spiral and b is adjusted to obtain a desired number of samples. It is shown that $t_h = 0.8$ leads to spirals whose performance approximates those patterns generated from $p_F(m, n)$. Here it is assumed that the MRI gradient hardware is designed such that the slew-rate and amplitude constraints allow the sampling trajectory to move from one sampling point to its neighboring points on the sampling grid without any difficulty [16].

4.3 Sampling in the ordered DHT domain

Sampling in the ordered Discrete Hadamard Transform (DHT) domain is suitable for image sampling with hardware capable of representing binary measurement matrices since the basis images of 2D ordered DHT are binary. Furthermore, ordered DHT has fast transform algorithms. In ordered DHT, the atoms are ordered by the number of sign changes (zero crossing) between consecutive entries in a Hadamard atom [8]. Thus, ordered DHT can be regarded as a generalized class of DFT and more specifically, a binarized version of DCT sharing thus many properties of DFT and DCT [17].

To design the incoherent sampling pattern in the ordered DHT domain, we need to exploit the fact that ordered DHT can be regarded as a binary approximation of the DCT. For illustrative purposes, we first describe the spectrum characteristics of 1D wavelets in the DCT domain. Let $v_{k,l}(m)$, $0 \leq m \leq N - 1$ be the DCT of a 1D wavelet $\varphi_{k,l}(n)$, $n = 0, 1, \dots, N - 1$. Define the averaged DCT spectrum of wavelets at scale k as:

$$V(m)_k = \sum_{l=0}^{N2^{-k}-1} |v_{k,l}(m)|. \quad (11)$$

It can be shown that the DCT spectrum of wavelets at scale k has approximately the same shape as their Fourier spectra. The DCT spectrum band $\tilde{\mathcal{B}}_k$ of wavelets at scale k is $\tilde{\mathcal{B}}_k \approx [N2^{-k}, N2^{-k+1}]$. Similar to incoherent subband sampling in the Fourier domain, to reconstruct $\varphi_{k,l}$ from its DCT samples, we need to select the DCT atoms randomly within the band $\tilde{\mathcal{B}}_k$. Now consider the incoherent sampling in the ordered DHT domain. We can define the averaged ordered DHT spectrum of wavelets at scale k as:

$$H(m)_k = \sum_{l=0}^{N2^{-k}-1} |h_{k,l}(m)|, \quad (12)$$

where $h_{k,l}(m)$, $0 \leq m \leq N - 1$, is the ordered DHT of $\varphi_{k,l}(n)$. Since ordered DHT is a binary approximation of the DCT, $H(m)_k$ can be approximated as: $H(m)_k \approx V(m)_k$. Figure 12 shows $H(m)_k$ for $k = 1$ to 4 where $N = 256$ and the underlying wavelets are Daubechies-4 wavelets. The corresponding DCT spectrum at scale k is also shown. It can be seen that

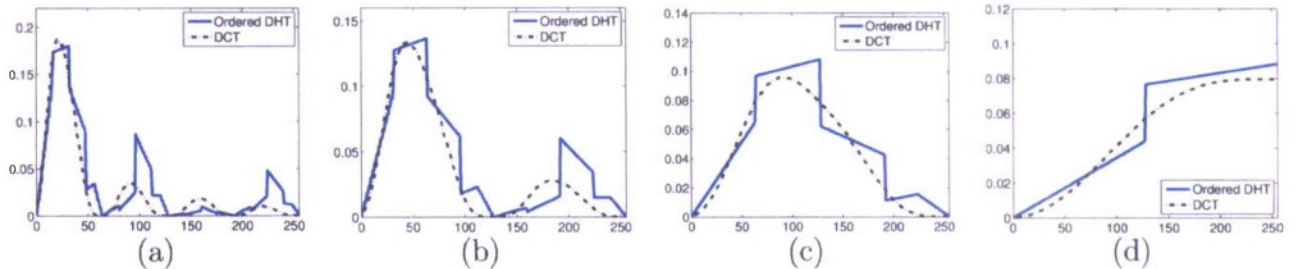


Figure 12: Ordered DHT and DCT spectra of Daubechies-4 wavelets. (a) at scale 4; (b) at scale 3; (c) at scale 2; (d) at scale 1.

the averaged ordered DHT spectrum and the averaged DCT spectrum are similar, which indicates that the principles of sampling in the DCT domain should be equally applied to the sampling in the ordered DHT domain. The above analysis can be readily applied to 2D cases. Following a similar procedure to that described in Sec. 4.2.1, the variable density sampling function in the 2D ordered DHT domain is designed as follows:

$$p_H(m, n) = \exp \left[-\frac{(\sqrt{(\frac{m}{M})^2 + (\frac{n}{N})^2})^{a_H}}{\sigma_H^2} \right], \quad (13)$$

where $0 \leq m \leq M-1$, $0 \leq n \leq N-1$. σ_H depends on the number of samples and a_H depends on the desired decay of the sampling probability. The sampling patterns are then obtained as realizations of $p_H(m, n)$. As sampling in the DFT domain, the sampling ratio is a monotonically increasing function of σ_H and searching of σ_H for a desired number of measurements is straightforward. Similar to (9), an initial guess of σ_H can also be found. As in Fourier sampling, simulation results show that $a_H \approx 1.3 a$ leads to good image reconstruction. If an estimation of a is not available, then setting $a_H = 3.5$ is also recommended.

4.4 Simulations Reconstruction Algorithm

In this section, extensive simulations are provided to illustrate the effectiveness of the proposed methods. The selection of the design parameters are also discussed. In the simulations, all the images are assumed sparse in the Daubechies-8 wavelet domain and pixel values are within $[0, 1]$. It is also assumed that each measurement is corrupted by additive white Gaussian noise with variance $\sigma^2 = 1e^{-4}$. The BPDN algorithm is used for image reconstruction.

In the first example, the proposed variable density sampling is applied to MRI image acquisition and reconstruction. The MRI images to be measured, *Brain* and *Angiography*, are of size 256×256 and are shown in Fig. 13(a) and Fig. 13(b), respectively. The estimated parameter a for each image is 2.32 and 2.47, respectively. The sampling patterns under investigation contains 15000 samples and there are 15000 real-valued measurements made along with each sampling pattern. Figure 13(c) shows the proposed single-shot spiral sampling pattern for fast MRI. The parameters of the spiral trajectory is set as: $a_F = 3.5$, $t_h = 0.8$, $\gamma = 47$ and $b = 4.5 \times 10^{-11}$. To generate the spiral pattern with continuously located sampling points, the sampling interval along t is set as: $\Delta t = 0.007$. Figure 13(h) shows part of the reconstructed *Brain* image corresponding to the region within the white frame in Fig. 13(a). It is clear that with an undersampling ratio of 22.9%, the MRI image is reconstructed with only small distortion. Figure 13(d) shows an example of the sampling pattern generated directly from the proposed sampling function given by Eq. (8) with

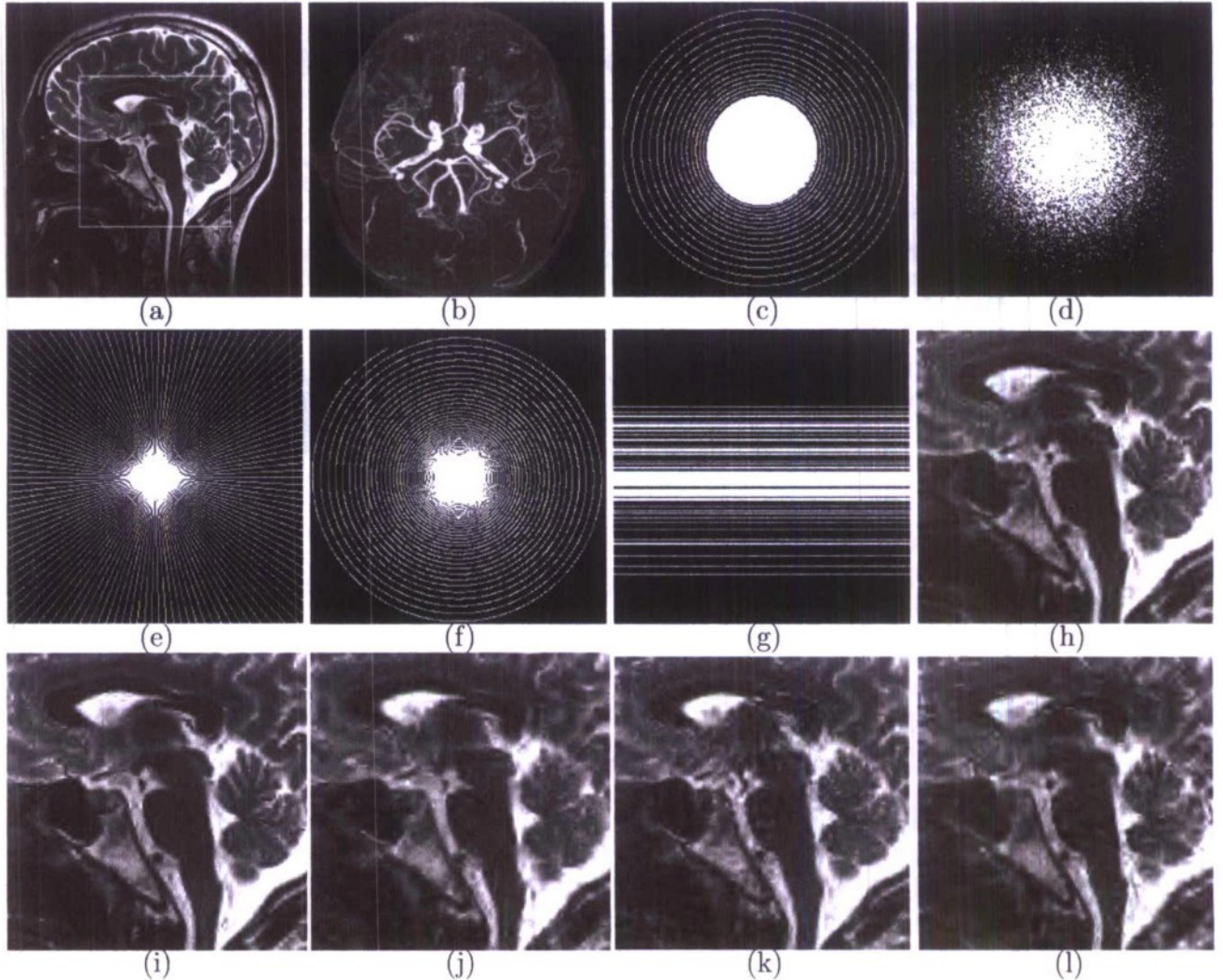


Figure 13: The original MRI images: (a) *Brain*; (b) *Angiography*. (c) Proposed single-shot spiral sampling pattern. (d) Proposed variable density sampling pattern. (e) Radial sampling pattern. (f) Logarithmic spiral pattern. (g) Random phase-encodes undersampling pattern. Each sampling pattern has a 22.9% undersampling ratio. Part of the reconstructed image with (h) proposed spiral sampling pattern; (i) proposed variable density sampling pattern; (j) radial sampling pattern; (k) logarithmic spiral pattern. (l) random phase-encodes undersampling pattern. See Table 1 for corresponding PSNR.

$a_F = 3.5$ and $\sigma_F = 0.134$, whose performance serves as a benchmark for the proposed spiral patterns. The corresponding reconstructed image is shown in Fig. 13(i), which contains less distortion than Fig. 13(h).

To compare the proposed sampling patterns with other practical sampling patterns, we also reconstruct the MRI image from samples taken from radial sampling pattern, logarithmic spiral sampling pattern and random phase-encodes undersampling pattern shown in Fig. 13(e), Fig. 13(f) and Fig. 13(g), respectively. The random phase-encodes undersampling is restricted to undersampling of the phase-encodes and fully sampled readouts and the sampling density scales according to a power of distance [7]. The corresponding recon-

Table 1: Reconstruction of MRI images. The performance is measured by PSNR (dB). “P. VD” is the proposed variable density sampling; “P. SS” is the proposed single-shot spiral sampling; “P-E U.” is the phase-encodes undersampling.

No.	P. VD	P. SS	Radial	Log-spiral	P-E U.
<i>Brain</i>					
5000	21.03	19.78	16.26	17.19	17.15
10000	23.86	22.45	19.55	20.58	20.46
15000	25.56	24.74	22.46	23.40	22.99
20000	27.23	26.51	24.68	25.97	24.73
25000	28.77	28.32	27.05	28.10	27.01
<i>Angiography</i>					
5000	23.68	22.32	19.87	20.34	21.27
10000	26.02	25.07	22.89	23.85	23.39
15000	27.85	27.38	25.30	26.10	25.70
20000	29.74	29.34	27.25	28.54	27.73
25000	31.34	31.09	29.18	30.39	29.61

structed MRI images for the above sampling patterns are shown in Fig. 13(j), Fig. 13(k) and Fig. 13(l), respectively. All reconstructed MRI images show more low frequency interference and the image qualities are not as good as that of the proposed single-shot spiral sampling pattern.

Table 1 summarizes more extensive simulation results for the MRI test images reconstruction with different sampling patterns, where the number of measurements ranges from 5000 to 25000 (undersampling ratio from 7.63% to 38.12%). The quality of the reconstructed images is measured by the peak signal to noise ratio (PSNR) and the data are collected from an average of ten runs. The results of the sampling patterns generated directly from the proposed sampling functions serve as the benchmarks and among all the sampling patterns, the best result is highlighted in bold font in each test set. The simulations again show that the proposed single-shot spiral sampling patterns consistently have better performance than other fast sampling patterns. The performance gain is 2 ~ 3 dB at $J = 5000$ and 0.2 ~ 0.7 dB at $J = 25000$ for both images. Furthermore, the difference in performance between the proposed single-shot spiral patterns and the sampling patterns generated from the proposed sampling density function is small.

In the second example, the proposed sampling method is applied to the acquisition and reconstruction of a set of natural images: *boat*, *Lena*, *Goldhill*, *baboon* and *Pentagon* with size 256×256 . The estimated parameter a for each images is estimated as: 2.65, 2.88, 2.32, 2.64, 2.27 and 2.05, respectively. Figure 14(b) shows a sampling pattern in the ordered DHT domain that contains 20000 sampling points generated from Eqn. (13) with $a_H = 3.5$ and $\sigma_H = 0.501$. Part of the reconstructed *boat* image corresponding to the region within the white frame in Fig. 14(a) is shown in Fig. 14(e), which shows that the reconstruction contains little distortion.

For comparison purposes, we also reconstruct the *boat* image from the samples taken from the radial sampling pattern and logarithmic spiral sampling pattern shown in Fig. 14(c) and Fig. 14(d), respectively. The number of measurements taken from both sampling patterns are the same as that of the proposed sampling pattern. Part of the corresponding reconstructed images are shown in Fig. 14(f) and Fig. 14(g), respectively. Again, both reconstructed images show more aliasing artifacts, which indicates that they are not as effective as the proposed

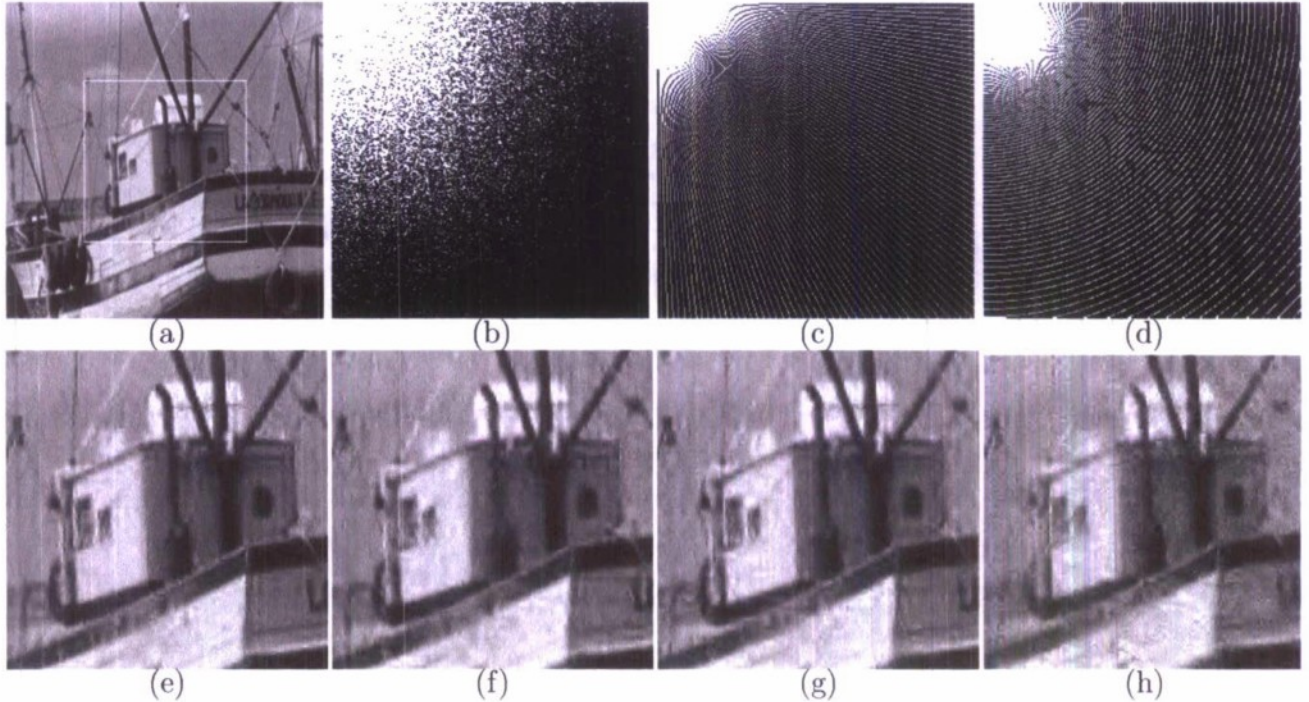


Figure 14: (a) The original image *Boat*. (b) Proposed variable density sampling pattern. (c) Radial sampling pattern. (d) Logarithmic spiral sampling pattern. Each sampling pattern has a 30.5% undersampling ratio. Part of the reconstructed image with (e) proposed variable density sampling pattern; (f) radial sampling pattern; (g) logarithmic spiral pattern; (h) SBHE. See Table 2 for corresponding PSNR.

sampling pattern.

Simulation results are summarized in Table 2, where the number of measurements ranges from 5000 to 25000 and the best results as the average of ten runs is also highlighted. For each test image, it is shown that the proposed variable density sampling achieves much better performance than logarithmic spiral patterns and radial patterns. The performance gain is $2 \sim 4$ dB at $J = 5000$ and $0.5 \sim 0.8$ dB at $J = 25000$. To verify that the proposed sampling pattern, which exploits the *a priori* information of natural images, achieves better performance than methods that do not exploit the *a priori* information, the simulation results using the Noiselet ensemble, SFE and SBHE under different number of measurements are also presented in Table 2. To acquire the image information, samples of the Noiselets, SFE and SBHE are taken randomly. The proposed sampling method achieves the best performance in all simulations. For illustrative purposes, Fig. 14(h) shows the reconstructed result for image *boat* using SBHE. Such comparison clearly shows the performance gain achieved by exploiting the *a priori* information.

Finally, we show that the reconstruction performance is not sensitive to the parameters a_p or a_H in the sampling functions. Here, we test the reconstruction performance as the parameter a_H changes. Figure 15 shows the reconstruction results of all test images with 20000 number of measurements. Data is collected as the result of 20 runs. Each test image has different curves and textures, thus has different statistical model parameters. The sampling

Table 2: Reconstruction of images in ordered DHT domain. The performance is measured by PSNR (dB). “P. VD” is the proposed variable density sampling.

No.	P. VD	Radial	Log-spiral	Noiselet	SFE	SBHE
<i>boat</i>						
5000	22.75	19.88	19.79	18.51	19.27	18.62
10000	24.93	22.93	22.77	20.78	21.39	20.74
15000	26.70	25.09	25.03	22.67	23.25	22.69
20000	28.36	26.96	26.95	24.19	24.93	24.56
25000	29.55	28.79	28.64	25.58	26.27	26.18
<i>Lena</i>						
5000	25.51	21.28	21.51	20.14	21.25	20.05
10000	27.91	25.33	25.49	23.10	23.87	23.10
15000	29.77	28.24	28.04	25.06	25.77	25.45
20000	31.24	30.07	29.91	26.76	27.56	27.43
25000	32.57	31.82	31.54	28.48	29.17	29.01
<i>Goldhill</i>						
5000	24.96	22.14	21.24	20.58	21.31	20.38
10000	27.09	25.14	24.80	22.89	23.36	22.81
15000	28.84	25.82	26.96	24.59	25.10	24.73
20000	30.18	27.30	28.67	25.98	26.59	26.52
25000	31.26	30.63	29.88	27.37	27.93	27.94
<i>baboon</i>						
5000	22.47	21.09	20.93	19.59	20.16	19.48
10000	23.32	22.55	22.57	21.08	21.36	20.91
15000	24.31	23.46	23.64	22.12	22.33	22.01
20000	25.30	24.60	24.67	23.04	23.36	23.05
25000	26.40	25.92	25.82	23.88	24.31	24.15
<i>pentagon</i>						
5000	24.78	22.59	22.69	21.37	21.95	21.32
10000	26.32	24.75	24.69	22.92	23.36	22.79
15000	27.61	26.32	26.19	24.33	24.54	24.17
20000	28.88	27.79	27.75	25.32	25.66	25.50
25000	29.86	28.13	28.97	26.22	26.87	26.77

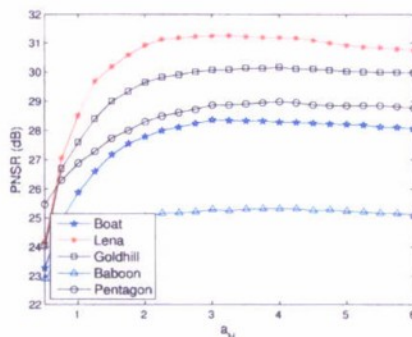


Figure 15: Reconstruction results of images from proposed sampling patterns generated by different a_H with 20000 number of measurements.

patterns are constructed with a_H ranging from 0.5 to 6. It shows that the sampling patterns lead to similar performance for all the images when a_H ranges from 2.5 to 4.5. The difference of performance measured by PSNR is within 0.4 dB. Thus, the image reconstruction is robust to variations over a_H . An empirical rule for the selection of a_H is $a_H = 1.3 a$. If the estimation of a is not available, then set $a_H = 3.5$ is recommended since $a_H = 3.5$ lies

in the middle of the flat region shown in Fig. 15. Note that the reconstruction performance tends to become worse as a_H increases. Since larger a_H means more low frequency samples are taken, the simulation shows that sampling only low frequency components is not a good strategy.

5 Conclusion

In this effort, we demonstrated the experimental realizations of different CS-based imaging systems. We first built a single pixel camera which captures 2-dimensional (2D) optical images using a single pixel detector. Based on the single pixel camera architecture, we built a CS-MSI system, which uses three beamsplitters and four single pixel detectors to acquire optical images at four spectral channels concurrently, including a red (650 nm), green (550 nm), blue (450 nm), and an NIR spectral channel. We also built a CS-based optical sectioning microscope (CSM), which used a single pixel detector to realize the optical sectioning imaging performance without any mechanical scanning. The optical sectioning imaging performance of the CSM system was demonstrated using a reflective imaging target and also a biological fluorescent specimen. A family of variable density sampling patterns are proposed for compressed sensing of natural images in the DFT, DCT and ordered DHT domain, which are based on a reliable statistical model of natural images in the sparse wavelet domain. The proposed sampling method is simple, fast and suitable for a wide range of applications such as in [18, 19]. Furthermore, the *a priori* information needed is general and no extensive data training is needed. Simulations show that the proposed sampling scheme is effective for compressed sensing of images conforming to the proposed wavelet model.

References

- [1] D. Donoho, "Compressed sensing," *IEEE Trans. Inf. Theory*, vol. 52, no. 4, pp. 1289–1306, Apr. 2006.
- [2] E. Candés, J. Romberg, and T. Tao, "Robust uncertainty principles: Exact signal reconstruction from highly incomplete frequency information," *IEEE Trans. Inf. Theory*, vol. 52, no. 2, pp. 489–509, Feb. 2006.
- [3] M. Elad, "Optimized projections for compressed sensing," *IEEE Trans. Signal Process.*, vol. 55, no. 12, pp. 5695–5702, Dec. 2007.
- [4] E. Candés and J. Romberg, "Sparsity and incoherence in compressive sampling," *Inverse Problems*, vol. 23, no. 3, pp. 969–985, 2007.
- [5] L. Gan, T. T. Do, and T. D. Tran, "Fast compressive imaging using scrambled block Hadamard ensemble," Preprint, 2008.
- [6] M. Lustig, D. Donoho, and J. M. Pauly, "Sparse MRI: The application of compressed sensing for rapid MR imaging," *Mag. Reson. in Med.*, vol. 58, no. 6, pp. 1182–1195, Dec. 2007.

- [7] C. Schröder, P. Börnert, and B. Aldefeld, "Spatial excitation using variable-density spiral trajectories," *J. Mag. Reson. Imag.*, vol. 18, no. 1, pp. 136–141, 2003.
- [8] Y. Q. Shi and H. Sun, *Image and video compression for multimedia engineering*, CRC press, 1999.
- [9] Emmanuel Candés, "Compressive sampling," *Int. Congress of Mathematics*, vol. 3, pp. 1433–1452, 2006.
- [10] D.L Donoho and X. Huo, "Uncertainty principles and ideal atomic decomposition," *IEEE Trans. Inform. Theory*, vol. 47, no. 7, pp. 2845–2862, Nov. 2001.
- [11] S. S. Chen, D. L. Donoho, and M. A. Saunders, "Atomic decomposition by Basis Pursuit," *SIAM SCI. Comput.*, vol. 20, no. 1, pp. 33–61, Aug. 1998.
- [12] S. Mallat, *A Wavelet tour of signal processing*, Academic Press, 1998.
- [13] S. G. Chang, B. Yu, and M. Vetterli, "Adaptive wavelet thresholding for image denoising and compression," *IEEE Tran. Image Process.*, vol. 9, no. 9, pp. 1532–1546, Sep. 2000.
- [14] J. K. Romberg, H. Choi, and R. G. Baraniuk, "Bayesian tree-structured image modeling using wavelet-domain hidden Markov models," *IEEE Trans. Image Process.*, vol. 10, no. 7, pp. 1056–1068, Jul. 2001.
- [15] J. L. Prince and J. M. Links, *Medical imaging signals and systems*, Pearson Prentice Hall, 2006.
- [16] S-J Kim M. Lustig and J. M. Pauly, "A fast method for designing time-optimal gradient waveforms for arbitrary k-space trajectories," *IEEE TMI*, vol. 27, no. 6, pp. 866–873, Jun. 2008.
- [17] N. P. Pitsianis, D. J. Brady, A. Portnoy, X. Sun, T. Suleski, M. A. Fiddy, M. R. Feldman, and R. D. Tekolste, "Compressive imaging sensors," in *Proe. SPIE*, 1999, vol. 6232.
- [18] J. L. Paredes, G. R. Arce, and Z. Wang, "Ultra-wideband compressed sensing: channel estimation," *IEEE J. STSP*, vol. 1, no. 3, pp. 383–395, Oct. 2007.
- [19] P. Ye, J. L. Paredes, G. R. Arce, Y. Wu, C. Chen, and D. W. Prather, "Compressive confocal microscopy," in *Proe. IEEE ICASSP*, Taiwan, 2009.

REPORT DOCUMENTATION PAGE

Form Approved
OMB No. 0704-0188

Public reporting burden for this collection of information is estimated to average 1 hour per response, including the time for reviewing instructions, searching data sources, gathering and maintaining the data needed, and completing and reviewing the collection of information. Send comments regarding this burden estimate or any other aspect of this collection of information, including suggestions for reducing this burden to Washington Headquarters Service, Directorate for Information Operations and Reports, 1215 Jefferson Davis Highway, Suite 1204, Arlington, VA 22202-4302, and to the Office of Management and Budget, Paperwork Reduction Project (0704-0188) Washington, DC 20503.

PLEASE DO NOT RETURN YOUR FORM TO THE ABOVE ADDRESS.

1. REPORT DATE (DD-MM-YYYY) 14/03/2011		2. REPORT TYPE Final Report		3. DATES COVERED (From - To) Dec. 2006 - June 2010	
4. TITLE AND SUBTITLE Compressed Sensing (CS) Imaging with Wide FOV and Dynamic Magnification				5a. CONTRACT NUMBER	
				5b. GRANT NUMBER N00014-07-1-0393	
				5c. PROGRAM ELEMENT NUMBER	
6. AUTHOR(S) Arce, Gonzalo R. Prather, Dennis W.				5d. PROJECT NUMBER	
				5e. TASK NUMBER	
				5f. WORK UNIT NUMBER	
7. PERFORMING ORGANIZATION NAME(S) AND ADDRESS(ES) Universtiy of Delaware 210 Hullihen Hall Newark, DE 19716				8. PERFORMING ORGANIZATION REPORT NUMBER ELEG33223507000	
9. SPONSORING/MONITORING AGENCY NAME(S) AND ADDRESS(ES) Office of Naval Research ONR Department Code: 312 875 North Randolph Street Arlington, VA 22203-1995				10. SPONSOR/MONITOR'S ACRONYM(S) ONR	
				11. SPONSORING/MONITORING AGENCY REPORT NUMBER	
12. DISTRIBUTION AVAILABILITY STATEMENT Approved for Public Release; Distribution is Unlimited.					
13. SUPPLEMENTARY NOTES					
14. ABSTRACT In this project we developed imaging systems based on the principles of compressive sensing. We developed advanced signal processing algorithms as well as a hardware testbed. The key idea in CS reconstruction is the realization that most signals encountered in practice are sparse in some domain and the theory of CS exploits such sparsity to dictate that far fewer sampling resources than traditional approaches are needed. Spectral image cubes are particularly well suited for sparse representation as images across different wavelengths exhibit strong correlation. We have thus developed a testbed to acquire and reconstruct natural images from a limited number of linear projection measurements at sub-Nyquist sampling rates. A key to the success of CS is the design of the measurement ensemble, which is based on the evaluation of the incoherence between the measurement ensemble and the sparsity basis. Due to the large scale nature of images, the generation of the measurement ensemble should be both computationally efficient and memory efficient. Based on these principles, we developed compressive cross-sectional imaging (confocal) systems, a single pixel compressive camera, and a multispectral imaging system. Advanced algorithms for the efficient reconstruction of the compressive measurements were developed.					
15. SUBJECT TERMS Compressive sensing; spectral imaging; sub-Nyquist sampling; image reconstruction; confocal imaging.					
16. SECURITY CLASSIFICATION OF:		17. LIMITATION OF ABSTRACT	18. NUMBER OF PAGES	19a. NAME OF RESPONSIBLE PERSON Gonzalo R. Arce	

INSTRUCTIONS FOR COMPLETING SF 298

a. REPORT U	b. ABSTRACT U	c. THIS PAGE U	UU	24	19b. TELEPHONE NUMBER (include area code) 302-831-1493
----------------	------------------	-------------------	----	----	---

--	--